



**HAL**  
open science

## Evaluation and improvement of IEC 60891 correction methods for I-V curves of defective photovoltaic panels

Baojie Li, Anne Migan-Dubois, Claude Delpha, Demba Diallo

### ► To cite this version:

Baojie Li, Anne Migan-Dubois, Claude Delpha, Demba Diallo. Evaluation and improvement of IEC 60891 correction methods for I-V curves of defective photovoltaic panels. *Solar Energy*, 2021, 216, pp.225-237. 10.1016/j.solener.2021.01.010 . hal-03237596

**HAL Id: hal-03237596**

**<https://centralesupelec.hal.science/hal-03237596v1>**

Submitted on 4 Nov 2021

**HAL** is a multi-disciplinary open access archive for the deposit and dissemination of scientific research documents, whether they are published or not. The documents may come from teaching and research institutions in France or abroad, or from public or private research centers.

L'archive ouverte pluridisciplinaire **HAL**, est destinée au dépôt et à la diffusion de documents scientifiques de niveau recherche, publiés ou non, émanant des établissements d'enseignement et de recherche français ou étrangers, des laboratoires publics ou privés.

# Evaluation and Improvement of IEC 60891 Correction Methods for I-V Curves of Defective Photovoltaic Panels

Baojie LI<sup>1,2</sup>, Anne MIGAN-DUBOIS<sup>1</sup>, Claude DELPHA<sup>2</sup>, Demba DIALLO<sup>1\*</sup>,

<sup>1</sup> Université Paris-Saclay, CentraleSupélec, CNRS, GeePs, Sorbonne Université, 3-11 Rue Joliot Curie, Gif Sur Yvette, 91192, France

<sup>2</sup> Université Paris-Saclay, CNRS, CentraleSupélec, L2S, 3 Rue Joliot Curie, Gif Sur Yvette, 91192, France

\* Corresponding author: [demba.diallo@centralesupelec.fr](mailto:demba.diallo@centralesupelec.fr)

**Abstract:** Correction of the I-V curve permits the comparison of curves measured under different conditions for photovoltaic (PV) panels' health monitoring purpose. IEC 60891 has defined three standard procedures named 1, 2 and 3 for the correction. They were initially designed to correct the curves of healthy PV panels. However, their performance, when applied to I-V curves measured on faulty panels, is rarely discussed. This work evaluates these correction methods on I-V curves simulated under different environmental conditions and for five types of defects of varying severity. The results show that procedure 3 has a relatively better overall performance but is not suitable for rapid application in the field as it requires the determination of reference curves. It is found that procedures 1 and 2 could introduce distortion of the curve's shape, with a relative error of up to 13.8 % and 6.4 %, respectively. A misestimation of 9.1 % for key parameters of the curve has been observed, when using procedure 2 for maximum power. Based on the performance analysis, a new correction method is proposed to fit the corrected voltage. It can reduce the curve's average correction error by 31.3 % compared to the original single curve correction method. Challenges and directions for future work are also presented.

**Key words:** Photovoltaic; I-V curve; I-V curve correction; IEC 60891; Fault detection and diagnosis;

Nomenclature			
$a$	Irradiance correction factor	$V_{oc}^{real}$	$V_{OC}$ of real curve at STC (V)
$\alpha$	Absolute temperature coefficient of $I_{SC}$ (A/°C)	$V_{rp}$	Voltage of inflexion point under PS (V)
$\alpha_{rel}$	Relative temperature coefficient of $I_{SC}$ (%/°C)	PS	Partial shading
$\beta$	Absolute temperature coefficient of $V_{OC}$ (V/°C)	$P_m$	Maximum Power (W)
$\beta_{rel}$	Relative temperature coefficient of $V_{OC}$ (%/°C)	PV	Photovoltaic
CE	Curve error (%)	OC	Open circuit
$G$	Global in-plane irradiance (W/m <sup>2</sup> )	RE	Relative error (%)
GainPS	Block gain used in simulation to control PS degree	$R_{OC}$	Resistance used in simulation for OC ( $\Omega$ )
$I$	Current (A)	$R_s$	Series resistance ( $\Omega$ )
$I^c$	Current of corrected curve (A)	$R_{s\_degra}$	Resistance used in simulation for Rs degradation ( $\Omega$ )
$I^{real}$	Current of real curve at STC (A)	$R_{SC}$	Resistance used in simulation for SC ( $\Omega$ )
$I_{MPP}$	Current at MPP (A)	$R_{sh}$	Shunt resistance ( $\Omega$ )
$I_{rp}$	Current of inflexion point under PS (A)	$R_{sh\_degra}$	Resistance used in simulation for Rsh degradation ( $\Omega$ )
$I_{SC}$	Short-circuit current (A)	SC	Short circuit
$I_{SC}^{real}$	$I_{SC}$ of real curve at STC (A)	STC	Standard test condition
I-V curve	Current-voltage characteristics	TC	Temperature coefficient
MPP	Maximum power point	$T_m$	Module temperature (°C)
$\kappa$	Curve correction factor	$\gamma$	Interpolation constant for correction method M3
$V$	Voltage (V)		
$V_{MPP}$	Voltage at MPP (V)		
$V_{OC}$	Open-circuit voltage (V)		
$V_{OC}^{STC}$	$V_{OC}$ under STC in healthy condition (provided in datasheet) (V)		

## 1. Introduction

The current-voltage characteristics (I-V curves) measured from a faulty photovoltaic (PV) module or array (from now on, termed as faulty I-V curve) contain valuable information on the health status (Fadhel et al., 2019; Li et al., 2019). For a single module or small-scale PV string, one I-V tracer device can measure I-V curves under various meteorological conditions (Sarikh et al., 2020; Zhu and Xiao, 2020). Hardware solutions (integrated at inverter level) (Spataru et al., 2015) support are now commercially available to measure I-V curves at array or power plant level (Huawei, 2020). Therefore, with the increasing availability of field-measured I-V curves, I-V curves for PV health monitoring are becoming a hot topic (Mellit et al., 2018; Pillai and Rajasekar, 2018).

32 Based on a field-measured I-V curve under any environmental conditions, there are two common ways (Mellit et al., 2018;  
33 Pillai and Rajasekar, 2018) to use it for PV health monitoring and diagnosis:

- 34 • *Model-based difference analysis*: Analyze the residue between the measured I-V curve (or the extracted features) and  
35 the simulated ones for identical environmental condition,
- 36 • *Correction-based analysis*: Correct the whole measured I-V curve (or the extracted features) to specific environmental  
37 condition (generally Standard Test Condition (STC) (1000 W/m<sup>2</sup> and 25 °C)).

38 It is clear that for a model-based difference analysis, it is unnecessary to correct the I-V curve, but a suitable and accurate  
39 PV model is required.

40 However, for correction-based analysis, correction of the I-V curve is an indispensable step to make curves measured  
41 under different environmental conditions comparable. Based on the corrected curves, the open-circuit voltage ( $V_{OC}$ ), short-  
42 circuit current ( $I_{SC}$ ), the voltage at the point of maximum power ( $V_{MPP}$ ), current ( $I_{MPP}$ ) and power ( $P_m$ ) are commonly  
43 extracted characteristics for fault diagnosis (Agrawal et al., 2020; Chen et al., 2017; Huang et al., 2019) or power loss  
44 analysis (Wang et al., 2020). Besides, equivalent series resistance ( $R_s$ ) or shunt resistance ( $R_{sh}$ ) are also commonly  
45 calculated from corrected curves to analyze the degradation mode of PV networks (Bouaichi et al., 2019; Silva et al.,  
46 2019).

47 In this sense, if there are significant errors in the corrected curves or the corresponding characteristics, the subsequent PV  
48 diagnosis's accuracy will be severely compromised. Therefore, correction of I-V curves plays a vital role in PV health  
49 monitoring.

50 There are no specific methods proposed for the correction of faulty I-V curves to the best of our knowledge. Consequently,  
51 most researchers adopt the original or simplified IEC 60891 (IEC 60891, 2009) correction procedures (Golive et al., 2019;  
52 Rajput et al., 2016). For example, several authors have adopted the procedure 1 in IEC 60891 to correct I-V curves  
53 measured under partial shading (PS) (Dolara et al., 2013), potential induced degradation (PID) (Martínez-Moreno et al.,  
54 2018), dust soiling (Tanesab et al., 2017, 2015), or hot spot (Ma et al., 2019). Besides, procedure 2 of IEC 60891 is also  
55 used to correct the I-V curves' key parameters (Chen et al., 2017). These parameters can then be used as inputs of a classifier  
56 (e.g., artificial neural network (ANN)) to automatically identify the fault types (PS, open circuit (OC), short circuit (SC),  
57 or shunt resistance degradation). Similar applications can also be found in (Zhu et al., 2018).

58 It should be noted that these methods based on the IEC 60891 standard have been all initially designed for the correction  
59 of curves measured from healthy PV panels. Moreover, in literature, the suitability of these methods correction of the I-V  
60 curves of defective panels is rarely studied, let alone whether the defects' characteristics are distorted by the correction and  
61 thus lead to a diagnostic error. All these issues are decisive for the diagnosis of PV faults (Triki-Lahiani et al., 2018). Thus,  
62 this paper aims to first evaluate the IEC 60891 methods' performance for the correction of faulty panels I-V curves. Then,  
63 based on IEC 60891 methods' performance analysis, an improved correction method will be proposed and evaluated.

64 The outline of the paper is as follows. Section 2 introduces the methodology from the simulation of faulty I-V curves,  
65 introduces the correction methods and performance evaluation metrics. Sections 3 and 4 present the correction performance  
66 using the single or multiple-curves-based methods, respectively. The comparison of these methods and guidance on future  
67 work are discussed in Section 5. Section 6 concludes the paper.

68

## 69 **2. Methodology for the evaluation of correction methods**

70 Since our target is to evaluate the error caused by the correction methods, it is essential to avoid the effects of other factors,  
71 like the measurement uncertainty on irradiance  $G$ , module temperature  $T_m$  and I-V curve, which could be up to 5 % (Friesen  
72 et al., 2018). Therefore, the curves to be corrected are generated in simulation rather than from field measurement to ensure  
73 all the correction formula parameters are real values, without any bias.

### 74 **2.1. Simulation of I-V curves**

#### 75 **2.1.1. Simulation model**

76 A PV array is modelled under Simulink® to address several fault types. The array consists of two strings in parallel, and  
77 each string of three mc-Si modules in series, as shown in Fig.1 (a). Each module comprises three strings of twenty cells  
78 and three bypass diodes, as shown in Fig.1 (b). Table 1 lists the detailed module parameters.

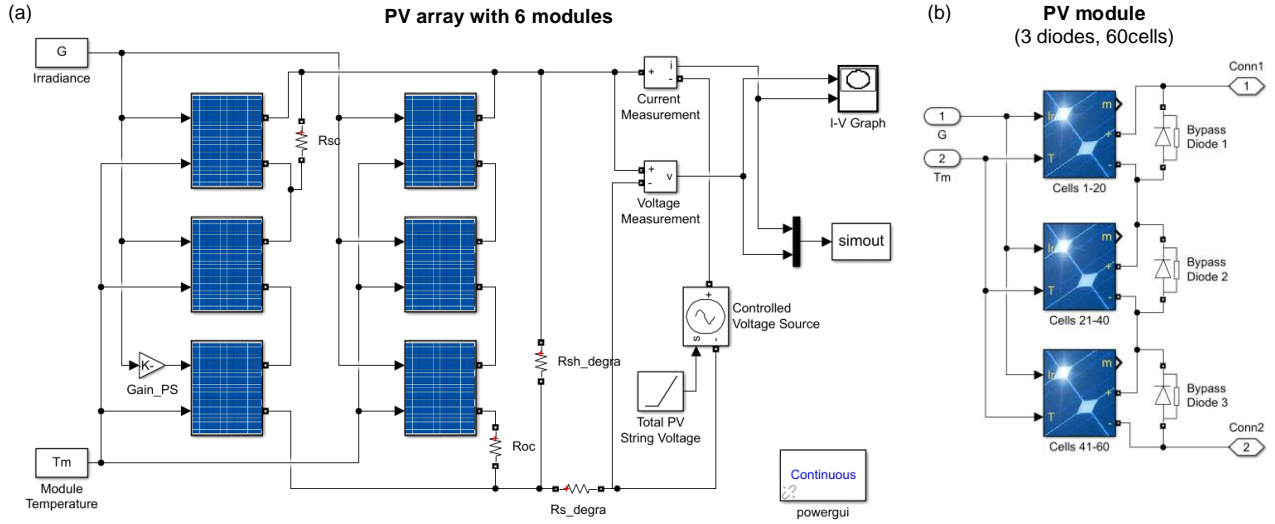


Fig. 1 Simulation model: (a) PV array structure, (b) PV module structure

Table 1 Parameter setting of mc-Si PV module

Variable	Value	Variable	Value
$I_{SC}$	8.64 A	$V_{MPP}$	31.80 V
$V_{OC}$	37.90 V	$\alpha_{rel}$	0.02 %/°C
$I_{MPP}$	6.52 A	$\beta_{rel}$	-0.36 %/°C

where,  $\alpha_{rel}$  and  $\beta_{rel}$  are the temperature coefficients (TC) of  $I_{SC}$  and  $V_{OC}$ , respectively.

The characteristics of the array's I-V curve depend on:

- $G$  and  $Tm$ : the values are identical for all the modules and depend on the correction methodology, which will be detailed in Sections 3.1 and 4.1;
- Fault Parameters: the gain block and resistors added as shown in Figure 1 (a), which are detailed as follows.

### 2.1.2. Configuration of faults

With the gain block and the additional resistors, the model can simulate PV array under healthy and faulty conditions. In this work, five typical faults are considered:

- 1) Partial shading (PS): 1 module is shaded by adjusting the value of the GainPS coefficient which varies in the range [0, 1] and controls the irradiation of the module ;
- 2) Short-Circuit (SC): 1 module is short-circuited by connecting the resistance  $R_{SC}$  in parallel;
- 3) Open-Circuit (OC): 1 string is open-circuited, by connecting the resistance  $R_{OC}$  in series;
- 4) Rs degradation (Rs degra): the equivalent series resistance of the array is increased by putting in series additional resistance  $R_{s\_degra}$ ;
- 5) Rsh degradation (Rsh degra): the equivalent shunt resistance of the array is decreased by connecting in parallel the resistance  $R_{sh\_degra}$ ;

Table 2 summarizes the different fault parameters and their corresponding range of variation used to analyze the impact of fault severity on the correction performance, presented in sections 3.2 and 4.2.

Table 2 Parameter setting for the different conditions

Condition	GainPS	$R_{SC}$ ( $\Omega$ )	$R_{OC}$ ( $\Omega$ )	$R_{s\_degra}$ ( $\Omega$ )	$R_{sh\_degra}$ ( $\Omega$ )
Healthy	1	$10^5$	$10^{-5}$	$10^{-5}$	$10^5$
PS 1 module	[0-1]	$10^5$	$10^{-5}$	$10^{-5}$	$10^5$
SC 1 module	1	$10^{-5}$	$10^5$	$10^{-5}$	$10^5$
OC 1 string	1	$10^5$	$10^5$	$10^{-5}$	$10^5$
Rs degradation	1	$10^5$	$10^{-5}$	[ $10^{-5}$ -2]	$10^5$
Rsh degradation	1	$10^5$	$10^{-5}$	$10^{-5}$	[ $10^5$ -10]

## 103 2.2. Correction methods

104 Through the literature review, the most common I-V curve correction methods are based on three procedures (hereafter,  
105 called M1, M2, and M3) proposed in IEC 60891 (IEC 60891, 2009). These methods and a proposed M2-based improved  
106 method are detailed as follows:

- 107 • Method 1 (M1):

$$108 \quad I_2 = I_1 + I_{SC1}(G_2/G_1 - 1) + \alpha(T_{m2} - T_{m1}) \quad (1)$$

$$V_2 = V_1 - R_s(I_2 - I_1) - \kappa I_2(T_{m2} - T_{m1}) + \beta(T_{m2} - T_{m1}), \quad (2)$$

109 where,  $I_1$  and  $I_2$ ,  $V_1$  and  $V_2$ ,  $T_{m1}$  and  $T_{m2}$ ,  $G_1$  and  $G_2$  are the current, voltage, module temperature, and irradiance  
110 before, and after correction, respectively;  $I_{SC1}$  is the short-circuit current before correction;  $\alpha$  and  $\beta$  are the PV module  
111 absolute TC of  $I_{SC}$  and  $V_{OC}$ , respectively;  $\alpha = \alpha_{rel} \cdot I_{SC}^{STC}$ ,  $\beta = \beta_{rel} \cdot V_{OC}^{STC}$ ,  $\alpha_{rel}$  and  $\beta_{rel}$  are the relative TC of  $I_{SC}$   
112 and  $V_{OC}$  (presented in Table 1);  $R_s$  is the internal series resistance and  $\kappa$  is the curve correction factor.

- 113 • Method 2 (M2):

$$114 \quad I_2 = I_1(1 + \alpha_{rel}(T_{m2} - T_{m1}))G_2/G_1 \quad (3)$$

$$V_2 = V_1 + V_{OC1}[\beta_{rel}(T_{m2} - T_{m1}) + a \cdot \ln(G_2/G_1)] - R_s(I_2 - I_1) - \kappa \cdot I_2(T_{m2} - T_{m1}), \quad (4)$$

115 where,  $V_{OC1}$  is the  $V_{OC}$  before correction;  $a$  is the irradiance correction factor;  $R_s$  and  $\kappa$  are determined by the  
116 procedure described in (IEC 60891, 2009).

117 The determination of the coefficients  $a$ ,  $R_s$  and  $\kappa$  for M1 and M2 requires a group of I-V curves at the same  $G$  or at the  
118 same  $Tm$ , which is troublesome and time-consuming to fulfill in real life. Therefore, in most M1 and M2 applications, these  
119 coefficients are either tuned via simulation under healthy condition (Silva et al., 2019) or neglected (Dolara et al., 2013)  
120 but to the detriment of lower performance. Therefore, in this paper, these coefficients will not be neglected and determined  
121 following the standard routine, i.e., via the simulation under healthy condition.

- 122 • New Method 2 (NewM2):

123 In fact, as it will be shown later, M1 and M2 do not perform well under all the tested faulty conditions. Thus, a new method  
124 denoted NewM2 is proposed. It uses the same formula as M2 for current correction. But for the voltage correction, the term  
125 ' $V_{OC1}$ ' in (4) is replaced by ' $V_{OC1}[1 + \beta_{rel}(25 - T_1)]$ '. The reason for this change will be explained in Section 3.2.1 while  
126 analyzing the correction performance. Therefore, the equations for NewM2 are:

$$127 \quad I_2 = I_1(1 + \alpha_{rel}(T_{m2} - T_{m1}))G_2/G_1 \quad (5)$$

$$V_2 = V_1 + V_{OC1}[1 + \beta_{rel}(25 - T_1)][\beta_{rel}(T_{m2} - T_{m1}) + a \cdot \ln(G_2/G_1)] - R_s(I_2 - I_1) - \kappa \cdot I_2(T_{m2} - T_{m1}) \quad (6)$$

- 128 • Method 3 (M3):

129 Different from M1, M2 or the NewM2, M3 is free from correction coefficient but needs an interpolation constant  $\gamma$ :

$$130 \quad I_3 = I_1 + \gamma(I_2 - I_1) \quad (7)$$

$$V_3 = V_1 + \gamma(V_2 - V_1) \quad (8)$$

131 According to (IEC 60891, 2009), M3 requires at least 2 reference curves to obtain one corrected curve at specified  $G$  or  
132  $Tm$  by calculating  $\gamma$  using (7) or (8). Thus, to correct a curve with a requirement on both  $G$  and  $Tm$ , three curves are  
133 necessary.

$$134 \quad G_3 = G_1 + \gamma(G_2 - G_1) \quad (9)$$

$$T_3 = T_1 + \gamma(T_2 - T_1) \quad (10)$$

135 In summary, the implementation of M1, M2, and NewM2 only requires one single I-V curve, while M3 requires multiple  
136 curves. Since their correction procedures are different, their evaluation performance will be conducted separately (in  
137 Sections 3 and Section 4, respectively). Since STC ( $G = 1000 \text{ W/m}^2$  and  $Tm = 25 \text{ }^\circ\text{C}$ ) is more commonly adopted as the  
138 target condition for I-V curve-based diagnosis, in the following, if not stated, the correction of I-V curves refers to the  
139 correction to STC.

## 140 2.3. Performance evaluation metrics

141 The evaluation of correction performance will be conducted from two aspects, i.e., from the whole I-V curve and single  
142 extracted parameters (e.g., maximum power  $P_m$ ,  $V_{OC}$  and  $I_{SC}$ ). Firstly, for the whole I-V curve, the curve error (CE) is  
143 adopted as the metric, calculated by the normalized root-mean-square error between the corrected curve and the one

144 simulated-at-STC (from now on called real curve). It should be noted that the real curve only means that  $G$  and  $T_m$  are at  
 145 STC, but the array condition could be either healthy or faulty.

$$146 \quad CE = \frac{\sqrt{\frac{1}{N} \sum_{i=1}^N (I_i^c - I_i^{real})^2}}{I_{SC}^{real}} \times 100 \% \quad (11)$$

147 where,  $I_i^c$  and  $I_i^{real}$  are the current values from the corrected and actual curve, respectively, for the same voltage  $V_i$ .  $V_i$   
 148 is the  $i^{\text{th}}$  element of the voltage vector consisting of  $N$  points linearly distributed in the interval between 0 and  $V_{max}$  with a  
 149 constant step ( $V_{max}$  is constant for all the conditions). The value of  $V_{max}$  can be set higher than  $V_{oc}$  in order to prevent  
 150 the voltage after correction from exceeding the set value. In this study,  $V_{max}$  is set as 120V and  $N$  at 100.  $I_{SC}^{real}$  refers  
 151 to the  $I_{SC}$  extracted from the real curve.

152 Then, regarding the parameters, the correction is evaluated with the relative error ( $RE$ ):

$$153 \quad RE_X = \frac{X^c - X^{real}}{X^{real}} \times 100 \% \quad (12)$$

154 where,  $X^c$  and  $X^{real}$  are the parameters from the corrected and real curve, respectively.  $X$  can be a data coming directly  
 155 from the curve (such as  $P_m$ ,  $V_{OC}$  or  $I_{SC}$ ) or one of the parameters of the single-diode model ( $R_s$  or  $R_{sh}$  for example)  
 156 whose evolution can be considered as a signature of a defect.

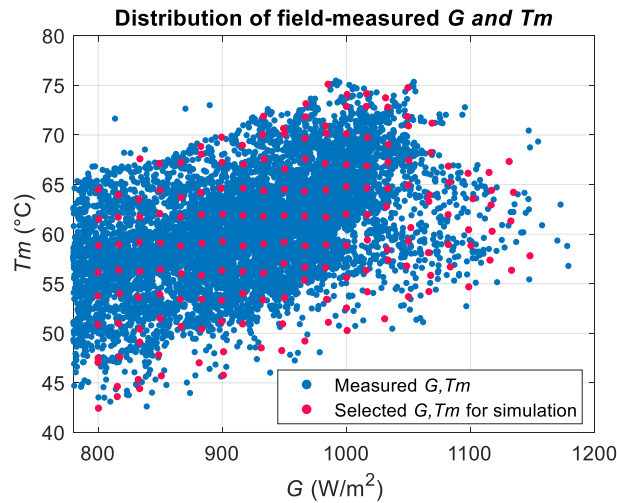
157

### 158 3. Performance of correction methods using single I-V curve

159 This section focuses on the correction methods based on a single I-V curve, i.e., M1, M2 and NewM2. Firstly, the selection  
 160 of  $G$  and  $T_m$  to generate the curves is presented in Section 3.1. Then, the correction performance (using the metrics  $CE$ ,  
 161 and  $RE$ ) will be evaluated using the curves simulated under constant or variable fault severity, presented in sections 3.2  
 162 and 3.3, respectively.

#### 163 3.1. Selection of $G$ and $T_m$ based on field measurement

164 To evaluate the correction methods with real environmental conditions, the selection of  $G$  and  $T_m$  to generate the curves is  
 165 based on field measurement (in SIRTa meteorological and climate observatory (Migan et al., 2015), France) of one mc-Si  
 166 PV module (identical to those used in the simulation in Section 2.1.1) during summer as illustrated in Fig. 2. To minimize  
 167 the correction error, commonly, the curves' irradiance for correction is selected in the highest range (Ding et al., 2014).  
 168 Therefore, in our case studies, the lower bound of  $G$  is set as 800 W/m<sup>2</sup>.



169  
 170 Fig. 2 Selected  $G$  and  $T_m$  based on field-measurement during summer for one mc-Si PV module

171 In Fig. 2, the blue points represent the measured  $G$  and  $T_m$ , while the red ones are selected for the simulation. A group of  
 172 174 pairs of  $G$  and  $T_m$  is selected based on a quasi-uniform distribution within the area enclosed by the blue points.

#### 173 3.2. Correction performance using curves for defects of constant severity

174 The fault severity is firstly set constant to investigate the impact of the selected  $G$  and  $T_m$ :

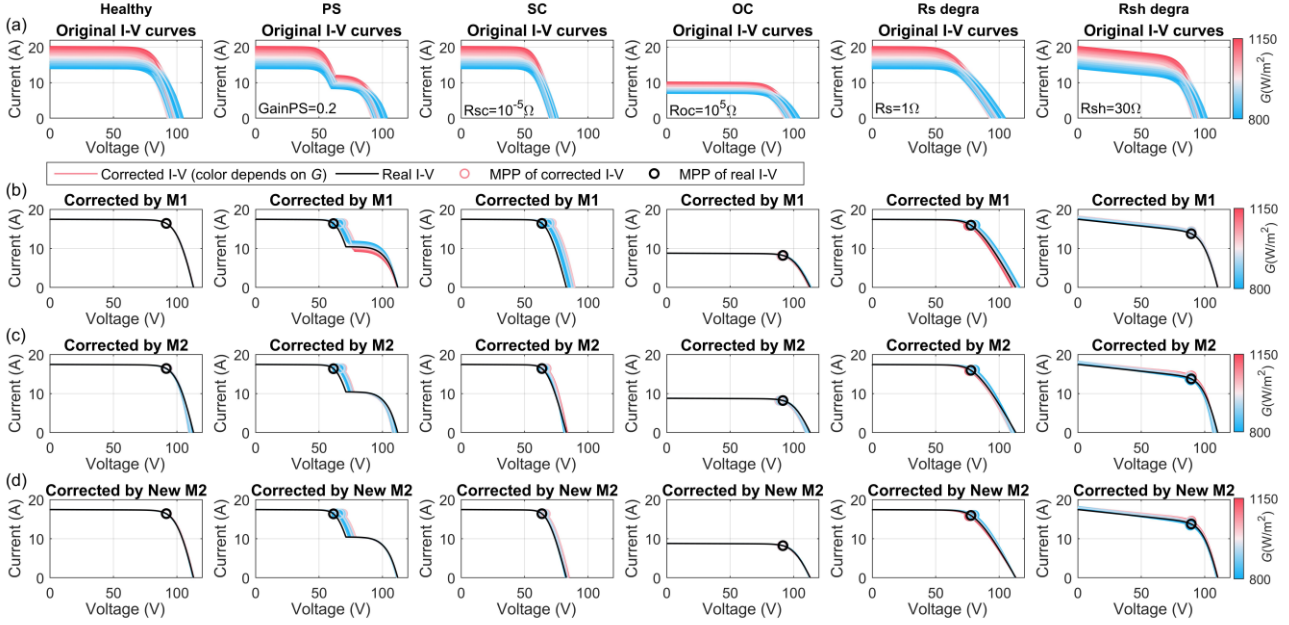
- 175 1) GainPS = 0.2 for partial shading,

- 176 2)  $R_s\_degra = 1 \Omega$  for series resistance degradation,  
 177 3)  $R_{sh\_degra} = 30 \Omega$  for shunt resistance degradation

178 Based on the generated curves, the correction performance can now be evaluated. Section 3.2.1 examines the shape of the  
 179 corrected curves. Section 3.2.2 analyzes the performance evaluation metrics  $CE$  and  $RE$  for key curve parameters, and  
 180 Section 3.2.3 studies the  $RE$  for the fault features.

### 181 3.2.1. Corrected I-V curve form

182 Using M1, M2 and NewM2, the curves before and after correction are displayed in Fig. 3.



183  
 184 Fig. 3 Correction results, (a): curves simulated for correction (each condition contains 174 curves with field-measured combinations of  
 185  $G$  and  $T_m$  at constant fault severity), (b): corrected curves using M1, (c): corrected curves using M2, (d): corrected curves using  
 186 NewM2 (the displayed color of each curve is determined by the irradiance value with the colorbar on the right side of the figure, the  
 187 circles on the curves represent the MPP)

188 For the corrected curves, apparent deviations to the real I-V curve can be observed for most faulty conditions using the  
 189 three methods. These deviations are due to the combined effect of voltage and current corrections, reflected along the  $x$   
 190 and  $y$  axes, respectively. They are now analyzed as follows:

#### 191 1) Voltage correction:

192 The deviations due to voltage corrections are observable in all the cases when using M2, but only for SC and  $R_s$  degradation  
 193 when using M1, and for SC when using the NewM2. To analyze these results, we rearrange the voltage correction formulas  
 194 (2), (4), and (6) as it follows:

$$195 V_2 = k_1 \cdot V_1 + k_2 \cdot (T_{m_2} - T_{m_1}) + k_3 \cdot \ln(G_2/G_1) + k_4 \cdot (I_2 - I_1) + k_5 \cdot I_2 \cdot (T_{m_2} - T_{m_1}), \quad (13)$$

196 where the different coefficients  $k_i$  ( $i = 1, \dots, 5$ ) for each method, are given in Table 3.

197 Table 3 Coefficients for voltage correction in M1, M2 and NewM2

Method	$k_1$	$k_2$	$k_3$	$k_4$	$k_5$
M1	1	$\beta_{rel} \cdot V_{OC}^{STC}$	0	$-R_s$	$-k$
M2	1	$\beta_{rel} \cdot V_{OC1}$	$a \cdot V_{OC1}$	$-R_s$	$-k$
NewM2	1	$\beta_{rel} \cdot V_{OC1} \cdot [1 + \beta_{rel}(T_{m_2} - T_{m_1})]$	$a \cdot V_{OC1}$	$-R_s$	$-k$

198 \* In this study, we correct the curves to STC, thus  $T_{m_2} = 25 \text{ }^\circ\text{C}$

199 Firstly, we compare M1 and M2. Based on the tuning procedure in the standard IEC 60891,  $k_4$  and  $k_5$  are similar for the  
 200 two methods. As for  $k_3$ , it is 0 in M1. In M2, since both the coefficient  $a$  and ' $\ln(G_2/G_1)$ ' are small values, their product  
 201 is a second-order term, and its contribution is negligible (within  $\pm 0.3 \%$ ). As a consequence, the main difference between  
 202 M1 and M2 lies in  $k_2$ . It is noteworthy that  $k_2$  for M1 is constant, while for M2, it depends on  $V_{OC1}$  ( $V_{OC}$  of the curve  
 203 to correct). In Fig. 3 (b), there is almost no distortion of the corrected curves when using M1 under healthy condition, which  
 204 demonstrates the voltage's correction efficiency. As for M2, since  $T_m$  of the curves to correct ( $T_{m_1}$ ) are all higher than

205 the target  $T_m$  ( $T_{m2}$ ,  $25^\circ\text{C}$ ),  $V_{oc1}$  is thus always lower than  $V_{OC}^{STC}$  (impact of  $G$  on  $V_{OC1}$  is negligible compared to  $T_m$ ).  
 206 Accordingly,  $k_2 \cdot (T_{m2} - T_{m1})$  in M2 is lower than in M1. Therefore, the corrected voltage in M2 is lower than in M1.  
 207 That is the reason why in Fig. 3 (c), we can observe the slight distortions of the corrected curves shifted on the left side of  
 208 the real curve round the open-circuit point.

209 Besides, the significant correction error under SC and PS for M1 and M2 also originates from the setting of  $k_2$ . For SC, to  
 210 be specific, short-circuit is introduced in one module of one string. As a consequence,  $V_{OC}^{real}$  is different from  $V_{OC}^{STC}$  (value  
 211 extracted from the datasheet, i.e., in healthy case), and is equal to around 2/3 of  $V_{OC}^{STC}$ . Therefore, in M1, the corrected  
 212 voltage is higher than the real value. As for M2,  $V_{OC1}$ , although varying with  $T_m$ , is still closer to  $V_{OC}^{real}$ . Consequently,  
 213 voltage correction is more efficient with M2. Regarding PS (1 module shaded), during the process of I-V scan, when the  
 214 bypass diodes get activated, the shaded module can be considered as a SC. That explains why a similar deviation is also  
 215 observed near the inflexion point.

216 From the above analysis, M1 and M2 have their pros and cons in voltage correction. Accordingly, NewM2 is designed by  
 217 combining their advantages. As observed before, in  $k_2$ , using  $V_{OC}^{STC}$  (like in M1) could generally lead to better voltage  
 218 correction than using  $V_{OC1}$  (like in M2) except under SC. The exception is because  $V_{OC}^{STC}$  fails to reflect  $V_{OC}^{real}$ . Therefore,  
 219 in NewM2,  $V_{OC1}$  is replaced by  $V_{OC1} \cdot [1 + \beta_{rel}(T_{m2} - T_{m1})]$ , which corrects the measured  $V_{OC1}$  to the  $V_{OC}$  under STC  
 220 of the real curve and therefore, could better approximate  $V_{OC}^{real}$  under any condition. In this way, as shown in Fig. 3 (d),  
 221 the correction errors near the open-circuit point using M1 (under SC) and using M2 (under other cases) are attenuated.

## 222 2) Current correction:

223 For the current of corrected curves, noticeable dispersion along the y-axis is observed under PS near the inflexion point  
 224 using M1. In fact, the output current of the PV module is mainly affected by  $G$ , while the impact of  $T_m$  is limited. Therefore,  
 225 to analyze this phenomenon, for simplification, the contribution of ' $(T_{m2} - T_{m1})$ ' is neglected. Then we can derive from  
 226 (1) and (3):

- 227 • For M1:

$$228 I_2 = I_1 + I_{SC1}(G_2/G_1 - 1) \quad (14)$$

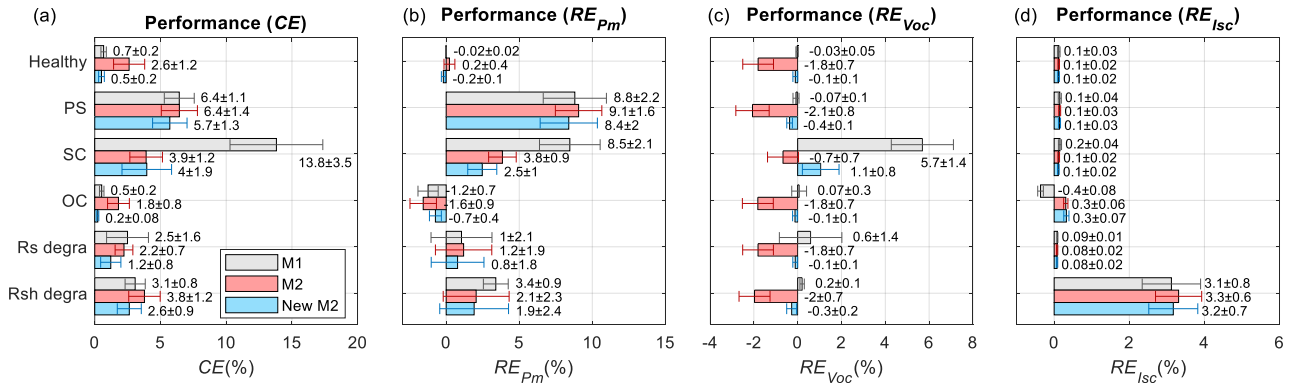
- 229 • For M2:

$$230 I_2 = I_1 \cdot G_2/G_1 \quad (15)$$

231 Comparing these two expressions, for M2, the corrected current ( $I_2$ ) is proportional to the current to correct ( $I_1$ ). While for  
 232 M1, there is always a bias that degrades correction's performance, particularly around the inflexion point, like in Fig. 3 (b)  
 233 under PS. Therefore, M2 performs relatively better than M1 in current correction. That also explains why, for NewM2, the  
 234 current formula of M2 is chosen, and the same performance is achieved in Fig. 3 (d).

## 235 3.2.2. CE and RE of key curve parameters

236 Based on the corrected curves, the performance evaluation metrics ( $CE$ ,  $RE_{P_m}$ ,  $RE_{V_{OC}}$  and  $RE_{I_{SC}}$ ) are calculated.  
 237 Considering that  $G$  and  $T_m$  are both varying for the 174 curves to correct, the statistics of the metrics are presented in Fig.  
 238 4.



239 Fig. 4 Four metrics to present the correction performance of M1, M2 and NewM2: (a)  $CE$ , (b)  $RE$  of  $P_m$ , (c)  $RE$  of  $V_{oc}$ , (d)  $RE$  of  
 240  $I_{SC}$  (the bars represent the mean value for the correction of 174 curves, while the horizontal whiskers represent the standard deviation  
 241 (std), these 2 values are marked as 'mean' ± 'std')  
 242

243 These metrics are analyzed as follows:

- 244 1)  $CE$ : The value of  $CE$ , which reflects the correction error on the whole curve, corresponds to the observations in  
 245 Fig. 3. As expected, high  $CE$  is found under SC using M1, and PS using all the methods. None of M1 and M2  
 246 outperforms in all the conditions, but the proposed NewM2 performs better with generally lower and more stable  
 247  $CE$ . The overall average  $CE$  (2.37 %) decreased by 31.3 % compared to the average when using M2 (3.45 %);
- 248 2)  $RE_{P_m}$ : Similarly, NewM2 performs better correction of  $P_m$ . However, it should be noticed that  $RE_{P_m}$  is positive  
 249 under nearly all the conditions for all the methods. This indicates that the fault impact on  $P_m$  is underestimated.  
 250 The mean maximum value is up to 9.1 %, which could hinder the detection of incipient PV fault if  $P_m$  is used as  
 251 a fault indicator;
- 252 3)  $RE_{V_{OC}}$ : The results are consistent with our previous observations, i.e., the corrected  $V_{OC}$  with M2 is always lower  
 253 than the real value under all conditions, while the  $V_{OC}$  using M1 is relatively better corrected except under SC,  
 254 where the maximum value of the mean  $RE_{V_{OC}}$  could reach 5.7 %. And NewM2 effectively reduces  $RE_{V_{OC}}$   
 255 compared with M1 (in SC), and M2 (in other cases);
- 256 4)  $RE_{I_{SC}}$ : The performance of the three methods is similar. It should be noted that, based on (2) and (4), the voltage  
 257 of the short-circuit point on the original curve (i.e., equals 0), after correction, is positive. This phenomenon is  
 258 also observed in (Bühler et al., 2014). Therefore, to retrieve the  $I_{SC}$  (according to the definition, the  
 259 corresponding voltage should be 0), the corrected curve must be extrapolated. Here, the extrapolation method in  
 260 (Bühler et al., 2014) is adopted. In this way, although the current value corrected from the original  $I_{SC}$  ( $I_{SC1}$ ) is  
 261 close to the actual  $I_{SC}$ , there is still a difference that depends on the initial slope of the corrected curve. Indeed for  
 262 all the conditions except Rsh degradation, where the slope is mild,  $RE_{I_{SC}}$  is low (within  $\pm 0.5$  %). But for Rsh  
 263 degradation, where the current at MPP is severely lowered down, the slope is steep, and  $RE_{I_{SC}}$  is larger.

### 264 3.2.3. RE of fault features

265 Now, we evaluate the correction performance from one or two typical curve parameters, selected as follows:

- 266 1) PS: The voltage and current at the inflexion point, named  $V_{rp}$  and  $I_{rp}$  respectively.  $I_{rp}$  could reflect the  
 267 shading level, and  $V_{rp}$  the number of activated bypass diodes of PV modules in one string;
- 268 2) SC: The open-circuit voltage  $V_{OC}$ ;
- 269 3) OC: The short-circuit current  $I_{SC}$ ;
- 270 4)  $R_s$  degradation: The extracted  $R_s$  from I-V curve,  $R_s = -\frac{1}{\frac{dI}{dV}|_{V=V_{OC}}}$  (Chin et al., 2015);
- 271 5) Rsh degradation: The extracted  $R_{sh}$  from I-V curve,  $R_{sh} = -\frac{1}{\frac{dI}{dV}|_{I=I_{SC}}}$  (Chin et al., 2015);

272 For each fault feature, the  $RE$  is calculated from the values obtained from the corrected and real curves. The results are  
 273 summarized in Table 4. We can observe large misestimation (absolute mean  $RE > 2$  %) with  $V_{rp}$ ,  $I_{rp}$ ,  $V_{OC}$  and  $R_s$  when  
 274 using M1, and  $V_{rp}$ ,  $R_s$  and  $R_{sh}$  when using M2 and NewM2. Worse yet, nearly all these large errors (except  $R_{sh}$  using  
 275 M2 and NewM2) lead to underestimating fault features, which will affect the detection of incipient faults. Similarly, none  
 276 of the three methods outperforms for all the fault features. However, the overall performance of NewM2 is relatively better.

277 Table 4 Impact of correction on fault features using M1, M2 and NewM2

Case	Fault feature	M1		M2		NewM2	
		Value (%) (mean $\pm$ std)	Impact on fault feature	Value (%) (mean $\pm$ std)	Impact on fault feature	Value (%) (mean $\pm$ std)	Impact on fault feature
PS	$RE_{V_{rp}}$	7.3 $\pm$ 2.6	Underestimated	6.8 $\pm$ 1.3	Underestimated	7.4 $\pm$ 1.8	Underestimated
	$RE_{I_{rp}}$	2.5 $\pm$ 6.6	Underestimated	-0.2 $\pm$ 0.1	Overestimated	-0.2 $\pm$ 0.1	Overestimated
SC	$RE_{V_{OC}}$	5.7 $\pm$ 1.4	Underestimated	-0.7 $\pm$ 0.7	Overestimated	1.1 $\pm$ 0.8	Underestimated
OC	$RE_{I_{SC}}$	-0.4 $\pm$ 0.08	Overestimated	0.3 $\pm$ 0.06	Underestimated	0.3 $\pm$ 0.07	Underestimated
Rs degra	$RE_{R_s}$	-3.4 $\pm$ 0.7	Underestimated	-13.6 $\pm$ 5.1	Underestimated	-5.5 $\pm$ 5.3	Underestimated
Rsh degra	$RE_{R_{sh}}$	-0.1 $\pm$ 0.4	Overestimated	-4.6 $\pm$ 9.0	Overestimated	-4.1 $\pm$ 9.1	Overestimated

278

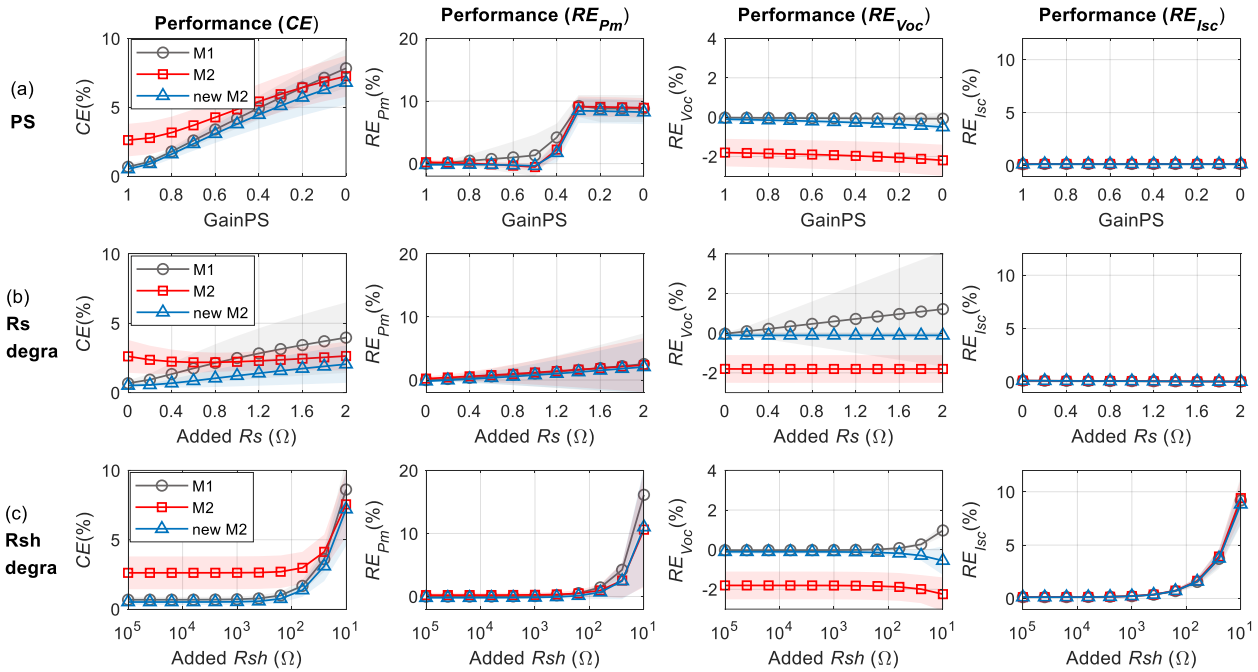
### 279 3.3. Correction performance using curves for defects of variable severity

280 In this subsection, the impact of each fault severity on correction performance is investigated. The severities of PS,  $R_s$ , and  
 281 Rsh degradations are varied in the following ranges one at a time: GainPS = 0:0.1:1,  $R_{s\_degra}$  = 10<sup>-5</sup>:0.2:2  $\Omega$  or  $R_{sh\_degra}$

282  $=10^{1:1.5} \Omega$ . For each fault level, the curves are simulated for the selected 174 pairs of  $G$  and  $Tm$  (presented in Section 3.1),  
 283 and corrected using the three single-curve based methods.

284 **3.3.1. CE and RE of key curve parameters**

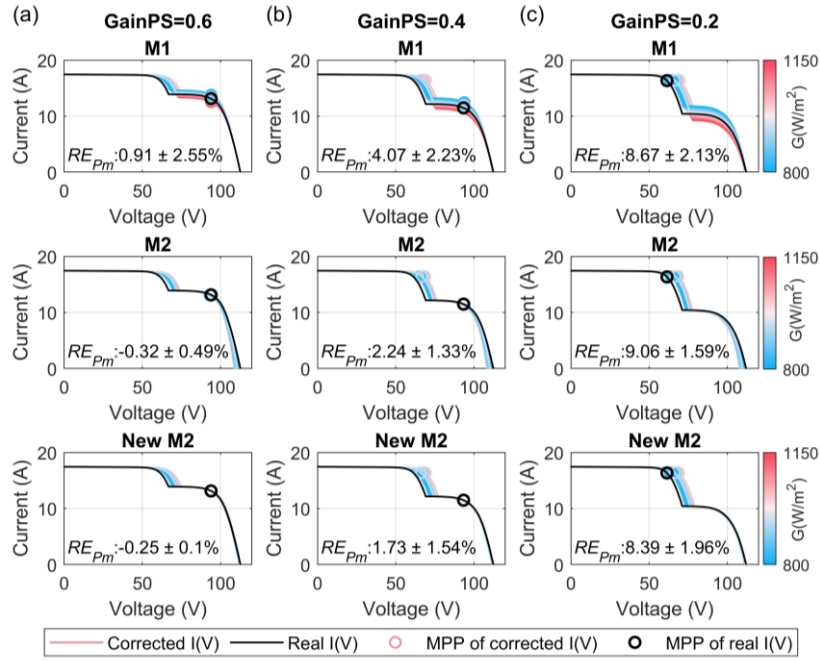
285 The performance metrics extracted from these corrected curves are now presented in Fig. 5 as a function of fault severity.



286  
 287 Fig. 5 CE and RE of  $P_m$ ,  $V_{oc}$  and  $I_{sc}$  using M1, M2 and NewM2 under 3 faulty conditions with variable fault severity: (a) PS, (b) Rs  
 288 degradation, (c) Rsh degradation (the marked line represents the mean of 174 values obtained from the correction of 174 under each  
 289 fault severity, while the band area behind represents the standard deviation; the  $x$ -axis for Rsh degradation is set as log scale; the  
 290 degree of severity is presented from healthy to severe on the  $x$ -axis from left to right)

291 From Fig. 5, several remarks can be drawn:

- 292 • All the metrics have a monotonic variation with the fault severities;
- 293 • CE is mainly sensitive to PS and severe Rsh degradation;
- 294 •  $RE_{P_m}$  is more sensitive to severe Rsh degradation and PS. The step variation observed for PS is due to the  
 295 maximum power point (MPP) shifting as it can be observed in Fig. 6;
- 296 •  $RE_{V_{oc}}$  and  $RE_{I_{sc}}$  are almost insensitive to all faults regardless of their level of severity, except for  $RE_{I_{sc}}$  under  
 297 severe Rs degradation;
- 298 • The overall performance of NewM2 is better than M1 and M2 with relatively lower CE and RE for key curve  
 299 parameters.



300

301

302

303

Fig. 6 Corrected curves and  $RE_{P_m}$  using M1, M2 and NewM2 under three fault severities of PS: (a) GainPS = 0.6, (b) GainPS = 0.4, (c) GainPS = 0.2 (the displayed color of corrected curves and MPP depends on the  $G$  of the curve to correct, the circles on the curves represent the MPP,  $RE_{P_m}$  are marked as 'mean'±'std')

304

305

306

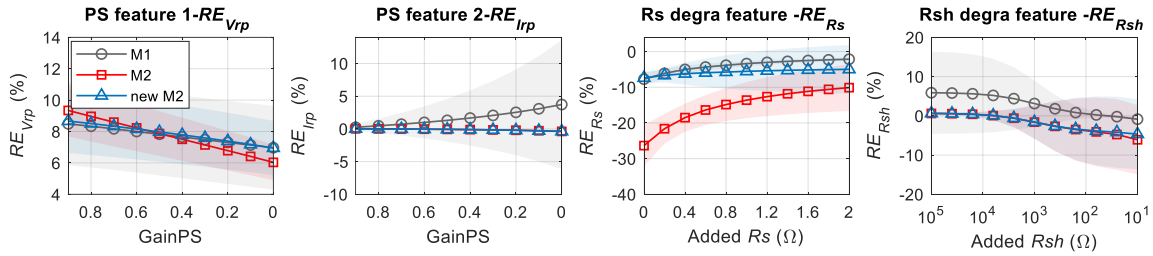
Moreover, it should be noted that, for  $P_m$ , which serves as an essential indicator for PV devices' health status, its  $RE$  is always positive and gradually increases with the fault severity. This means that using M1 or M2 leads to an inevitable underestimation of the fault impact, which increases with the fault severity.

307

### 3.3.2. $RE$ of fault features

308

The impact of fault severity on fault features is also investigated, as illustrated in Fig. 7.



309

310

311

312

313

Fig. 7  $RE$  of fault features under PS,  $R_s$  and  $R_{sh}$  degradations with variable fault severity (the marked line represents the mean of 174 values obtained from the correction of 174 curves under each fault severity, while the band area behind represents the standard deviation; the  $x$ -axis for  $R_{sh}$  degradation is set as log scale; the degree of severity is presented from healthy (except for  $V_{rp}$  and  $I_{rp}$  as these features do not exist under healthy condition) to severe on the  $x$ -axis from left to right)

314

315

316

317

Concerning the variation of the defect characteristics, different trends are observed: for the features  $V_{rp}$  and  $R_s$  using all the three methods and for  $R_{sh}$  using M1, the  $RE$  decreases as the severity of the defect increases. The opposite trend is observed for the other cases. This is due to the different changing rates of each feature's absolute error and its reference value, as defined in (12). Overall, NewM2 performs relatively better with lower and more stable  $RE$ .

318

319

320

It should be noted that within the range of severity of the defects tested; all characteristics are underestimated with the three methods. Therefore, used as defect signatures ( $R_s$  or  $R_{sh}$ , for example), which is typical for PV module degradation analyses, this could hamper the detection and diagnosis of these defects.

321

## 4. Performance of correction methods using multiple I-V curves

323

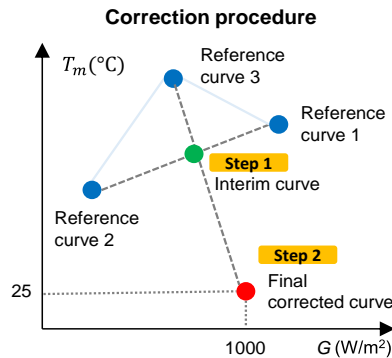
324

325

In this section, the method based on multiple curves (M3) will be evaluated. Section 4.1 presents the selection of  $G$  and  $T_m$  for the reference curves. Sections 4.2 and 4.3 present the correction performance using simulated curves with the selected  $G$  and  $T_m$ , for constant and then variable fault severity.

326 **4.1. Selection of  $G$  and  $T_m$  for reference curves**

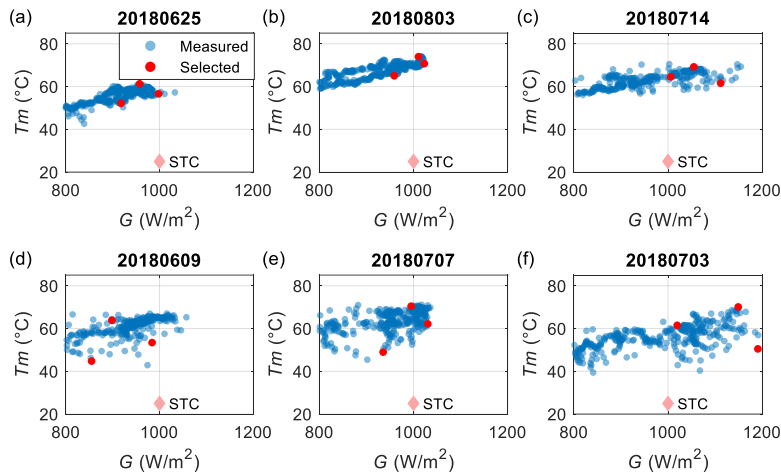
327 Different from M1 and M2, M3 needs at least three reference curves to complete one correction to STC. In this study, like  
 328 other common applications of M3, we apply the 2-step correction methodology proposed in (IEC 60891, 2009) with three  
 329 curves. An illustration of this methodology on  $G$ - $T_m$  plot is shown in Fig. 8.



330

331 Fig. 8 Illustration of 2-step correction methodology based on three curves (Step 1: use reference curves 1 and 2 to generate the interim  
 332 curve; Step 2: use reference curve 3 and the interim curve to get the final corrected curve)

333 Before the simulation of these curves,  $G$  and  $T_m$  need to be determined. The field-measured distributions of  $G$  and  $T_m$  of  
 334 the same mc-Si module employed in the simulation represent as many real situations as possible. As shown in Fig. 8, three  
 335 reference curves form one group of curves to get one corrected-to-STC curve. The irradiance  $G$  and temperature  $T_m$  of  
 336 these reference curves are determined by one-day measurement, covering sunny and cloudy conditions. The latter have  
 337 larger fluctuations of  $T_m$ . Besides, for sunny and cloudy conditions, three possible conditions are also considered for the  
 338 irradiance: 1) lower than 1000 W/m<sup>2</sup>, 2) around 1000 W/m<sup>2</sup> and 3) higher than 1000 W/m<sup>2</sup>. In total, 120 groups of  $G$  and  
 339  $T_m$  are manually selected. Some examples are shown in Fig. 9.



340

341 Fig. 9 Examples of selected  $G$  and  $T_m$  from different summer days: (a, b, c) clear sunny days, (d, e, f) cloudy days ((a, d): the 3  
 342 selected  $G < 1000$  W/m<sup>2</sup>, (b, e): selected  $G$  around 1000 W/m<sup>2</sup>, (c, f): selected  $G > 1000$  W/m<sup>2</sup>)

343

344 **4.2. Correction performance using field-measured  $G$  and  $T_m$  for defect of constant fault severity**

345 Firstly, we use the same fault configuration presented in Section 3.1 and simulate 120 groups of reference curves regarding  
 346 the fault severity setting. Then, M3 is applied to obtain 120 corrected curves, as shown in Fig. 10. The corresponding  
 347 performance metrics and fault features are summarized in Table 5.

348

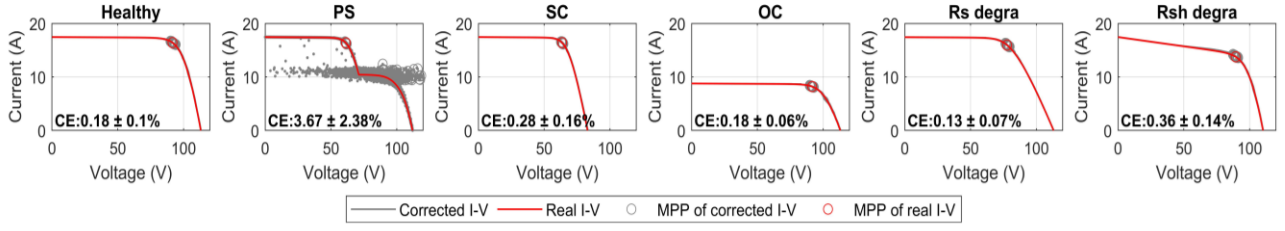


Fig. 10 Corrected curves using M3 (for PS, due to the large fluctuations, the corrected curves are plotted with dot line for better presentation)

Table 4 Four metrics to present the correction performance and the impact of correction on fault features using M3

Case	CE (%) (mean ± std)	$RE_{P_m}$ (%) (mean ± std)	$RE_{V_{OC}}$ (%) (mean ± std)	$RE_{I_{SC}}$ (%) (mean ± std)	Fault feature		
					Feature	Value (%) (mean ± std)	Impact on fault feature
Healthy	0.18±0.10	-0.02±0.1	0.07±0.04	$6.10^{-3}±0.05$	-	-	-
PS	3.67±2.38	7.5±18.3	0.06±0.07	$6.10^{-3}±0.05$	$RE_{V_{rp}}$	-6.9±32.0	Overestimated
					$RE_{I_{rp}}$	3.2±12.2	Underestimated
SC	0.28±0.16	0.03±0.3	0.2±0.1	$6.10^{-3}±0.05$	$RE_{V_{OC}}$	0.2±0.1	Underestimated
OC	0.18±0.06	2e-4±0.2	0.07±0.05	$6.10^{-3}±0.05$	$RE_{I_{SC}}$	$6.10^{-3}±0.05$	Underestimated
Rs degra	0.13±0.07	0.1±0.2	0.07±0.03	$6.10^{-3}±0.05$	$RE_{R_s}$	0.01±0.04	Overestimated
Rsh degra	0.36±0.14	0.4±0.2	0.05±0.04	$6.10^{-3}±0.05$	$RE_{R_{sh}}$	$4.10^{-3}±0.01$	Underestimated

From the results, clearly, except for PS, M3 achieves good correction (mean value of all metrics within  $\pm 1\%$ ) for all the conditions.

In the following, we analyze the ‘catastrophic’ correction error near the inflexion point under PS. As illustrated in Fig. 8, the correction procedure using M3 is done in two steps. An example of these steps under PS is shown in Fig. 11. In step 1, due to the unsynchronized appearance of inflexion points on reference curves 1 and 2 (i.e.,  $V_{rp}$  are not identical), another inflexion point is created on the intermediate curve, so that in step 2, a strange curve shape is introduced. This phenomenon could lead to a large error on  $P_m$  but with no significant impact on  $V_{OC}$  and  $I_{SC}$ .

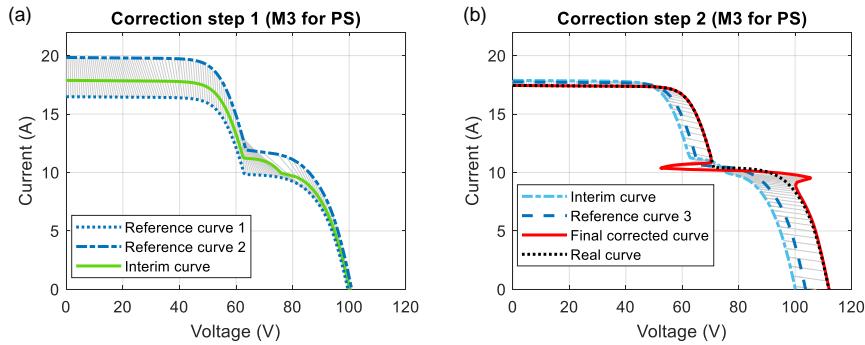
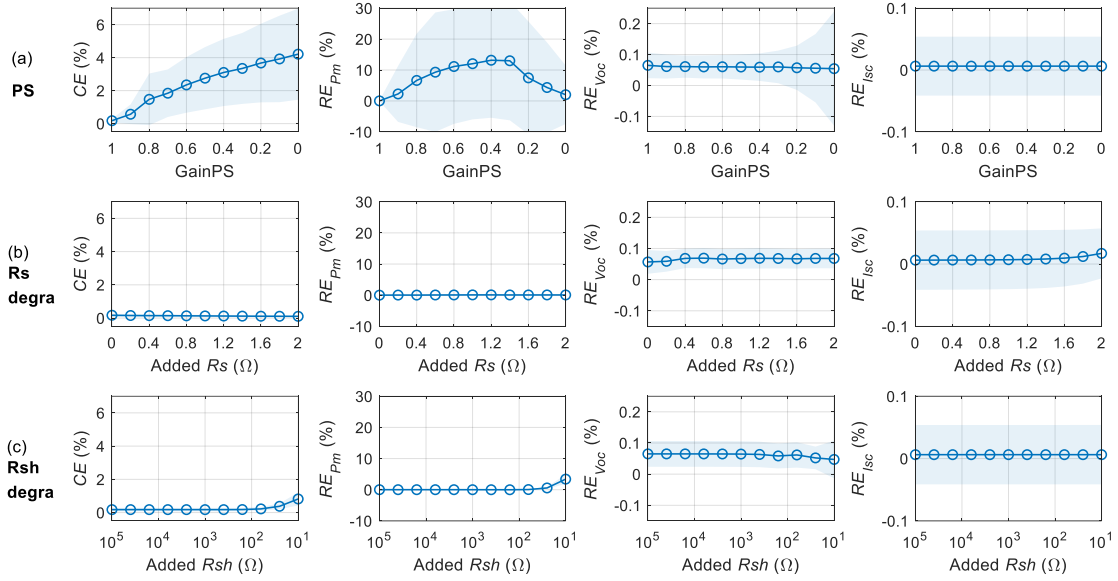


Fig. 11 Correction procedure under PS using 3 reference curves-based M3: (a) correction step 1, (b) correction step 2

Also, it should be noted that the fault impact on all the fault features is underestimated. Furthermore, as expected, the most significant error occurs under PS. Under the other conditions, the  $RE$  is within  $\pm 1\%$ .

### 4.3. Correction performance using field-measured $G$ and $T_m$ for defects of variable severity

In this subsection, the impact of fault severity on correction performance using M3 is investigated. The severity for PS, Rs and Rsh degradations is varied using the same setting as in Section 3.2. The performance metrics as a function of fault severity are presented in Fig. 12.



370

371 Fig. 12 CE and RE of  $P_m$ ,  $V_{oc}$  and  $I_{sc}$  for M3 under 3 faulty cases with variable fault severity: (a) PS, (b)  $R_s$  degradation, (c)  $R_{sh}$  degradation (the circled line represents the mean value for the 120 corrected curves for each fault severity, while the band area behind represents the standard deviation; the  $x$ -axis for  $R_{sh}$  degradation is set as log scale; the degree of severity is presented from healthy to severe on the  $x$ -axis from left to right)

372

373

374

375

376

377

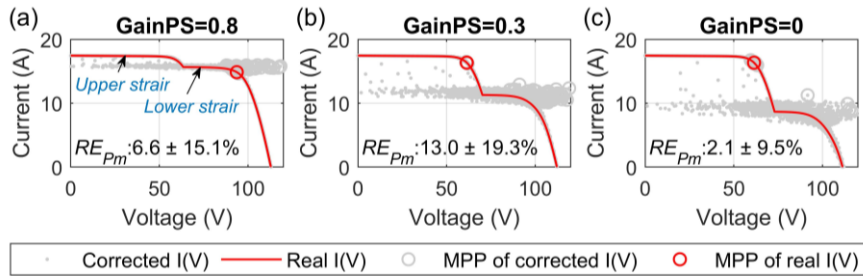
378

379

380

From these results, the following remarks could be drawn:

- Regarding  $R_s$  and  $R_{sh}$  degradations, all the metrics are insensitive to the fault level;
- Regarding PS, only  $CE$  and  $RE_{P_m}$  vary according to the fault severity.  $CE$  has a monotonic variation, which makes it relevant for fault severity estimation. However,  $RE_{P_m}$  is not a reliable feature as it exhibits a non-monotonic variation. This phenomenon is due to the displacement of the maximum power point (MPP) as illustrated in Fig. 13.



381

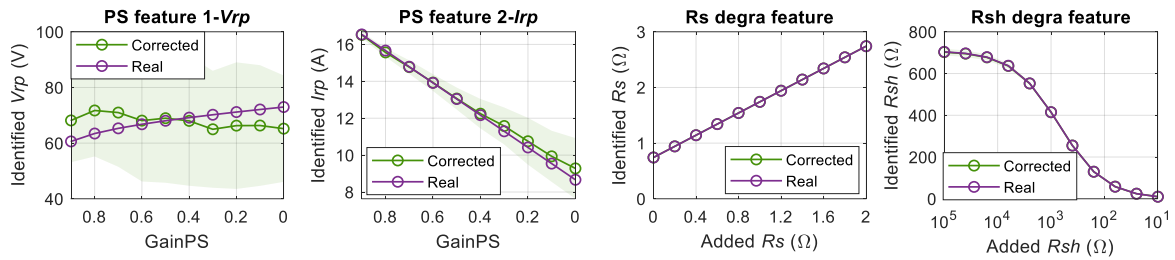
382 Fig. 13 Corrected curves using M3 under 3 fault severities of PS: (a)  $GainPS=0.8$ , where MPP of real and corrected curves are all at  
 383 'lower stair', (b)  $GainPS = 0.3$ , where MPP of real is at 'upper stair' while MPP of most corrected curves at 'lower stair' (c)  $GainPS =$   
 384 0, MPP of real and most corrected curves are all at 'upper stair' (for each case,  $RE_{P_m}$  is marked as 'mean'±'std')

385 The behavior of fault features is also investigated with the comparison of identified features from both corrected and real  
 386 I-V curves presented in Fig. 14 and the corresponding relative errors (RE) in Fig. 15.

387

388

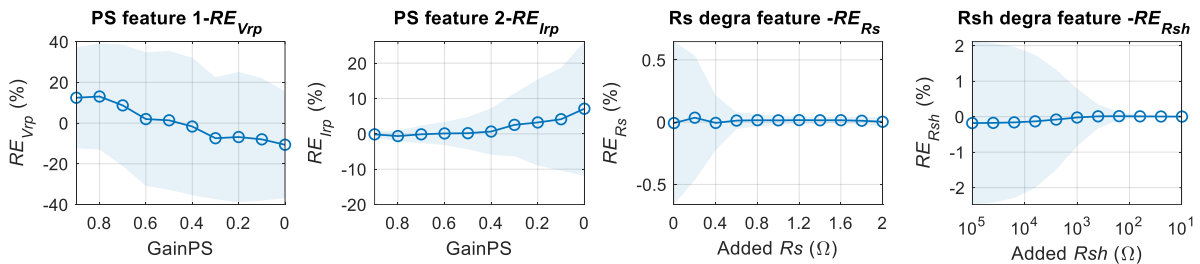
389



390

391 Fig. 14 Identified feature from corrected (using M3) and original I-V curve for fault of variable severity (the circled line represents the  
 392 mean, while the band area represents the standard deviation; the values of  $R_s$  or  $R_{sh}$  identified from I-V curve are not equal to the  
 393 additional resistance (illustrated in Fig. 1) due to the existence of inherent equivalent  $R_s$  ( $0.74 \Omega$ ) or  $R_{sh}$  ( $708.36 \Omega$ ) of PV arrays  
 394

395



396

397 Fig. 15 RE of fault features under PS,  $R_s$  and  $R_{sh}$  degradations for fault of variable severity using M3 (the circled line represents the  
 398 mean, while the band area represents the standard deviation)  
 399

400 The large dispersion observed for  $RE_{V_{rp}}$  and  $RE_{I_{rp}}$  confirms the poor performance of the correction near the inflexion  
 401 point. The values of  $R_s$  and  $R_{sh}$  extracted from the original and corrected curves are very close, as confirmed in Fig. 14.  
 402 This is also reflected in the low values of  $RE_{R_s}$  and  $RE_{R_{sh}}$  displayed in Fig. 15. The mean value of  $RE_{R_s}$  lies within  
 403  $\pm 0.1\%$  and that of  $RE_{R_{sh}}$  within  $\pm 0.2\%$ , and both are relatively insensible to the varying fault severity. It is also noted  
 404 that the standard deviations of  $RE_{R_s}$  and  $RE_{R_{sh}}$  exhibit a decreasing trend when the fault severity increases. In all, with  
 405 varying fault, M3 achieves quite good and robust correction under  $R_s$  and  $R_{sh}$  degradation.

406

## 407 5. Discussion

### 408 5.1. Summary of correction methods

409 The correction performance using three single and one multiple curves-based methods has been evaluated. Each method  
 410 has its own pros and cons listed in Table 6.

411

Table 6 Pros and Cons of correction methods

	Single curve-based methods			Multiple curves-based method (M3)
	M1	M2	NewM2	
Pros	<ul style="list-style-type: none"> <li>Better correction of voltage than M2</li> <li>Suitable for rapid field diagnosis</li> </ul>	<ul style="list-style-type: none"> <li>Better correction of current than M1</li> </ul>	<ul style="list-style-type: none"> <li>Better overall performance than M1 and M2</li> </ul>	<ul style="list-style-type: none"> <li>High-precision correction performance under most conditions</li> <li>Free of correction coefficients</li> </ul>
Cons	<ul style="list-style-type: none"> <li>Needs to determine the correction coefficients</li> <li>Prone to large underestimation of <math>P_m</math>, and fault features</li> </ul>			<ul style="list-style-type: none"> <li>Not suitable for rapid field diagnosis</li> <li>Needs at least 3 well-chosen reference curves</li> <li>Poor correction near inflexion point under PS with high effect on <math>P_m</math></li> </ul>

412

413 Once established (i.e., correction coefficients determined), all these single curve-based correction methods can conduct  
 414 rapid correction of measured I-V curves. This allows their integration in real-time health monitoring of PV devices.  
 415 However, as discussed in Section 2.2, the determination of correction coefficients is a troublesome task. The coefficients  
 416 determined using simulated data do not always fit the real values, especially for the installed PV panels after a long-time  
 417 operation. The proposed NewM2, which combines M1 and M2's advantages, leads to better correction performance in all

418 fault conditions tested. However, it still introduces a significant correction error in the case of partial shading (PS), the  
419 degradation of  $R_s$  and  $R_{sh}$ , compared to healthy conditions, short circuit (SC) and open circuit (OC).

420 As for the multiple-curves-based method (M3), except under PS, excellent correction is obtained. However, the selection  
421 of reference curves is still a manual process (Hishikawa et al., 2016; IEC 60891, 2009), which could hinder its application  
422 in rapid or on-line field correction.

## 423 **5.2. Suggestions for future work**

424 Based on comparing the three IEC 60891 correction methods and the new proposal, some suggestions on future work are  
425 hereafter presented.

426 For correction methods based on a single curve, the determination of correction coefficients for PV panels on-site remains  
427 difficult. A strategy for determining these coefficients based on field measured data needs to be developed that differs  
428 from the IEC 60891 procedure, which requires environmental conditions that are only practically feasible in fully equipped  
429 laboratories. Solutions to reduce dependence on correction coefficients, such as (Hishikawa et al., 2019, 2018), should  
430 also be further developed and validated with I-V curves taken from panels with defects.

431 The proposed new correction method still needs to be evaluated with more types of defects.

432 For the correction method based on multiple curves, two improvements are expected. On the one hand, efforts are needed  
433 to improve correction performance in case of partial shading; on the other hand, developing a methodology for automatic  
434 and efficient selection of reference curves would facilitate the deployment of the technique in the field.

435 Correction methods should be evaluated with field-measured data.

## 436 **6. Conclusion**

437 In this work, we have evaluated the performance of methods based on one or more curves proposed in the IEC 60891  
438 standard for the correction of I-V curves measured on defective photovoltaic panels. It has been shown that all the methods  
439 introduce significant errors due to irradiance, module temperature and the severity of the defects. Using the standard method  
440 M1 of the IEC, we have pointed out that a distortion of the curve's shape is commonly introduced with a relative error up  
441 to 13.8%. For  $P_m$  and the fault characteristics extracted from the corrected curves, estimation errors also occur frequently.  
442 Even worse still, most significant errors result in underestimating the characteristics (up to 9.1% for  $P_m$  using M2). This  
443 can affect the detection of incipient PV defects if these characteristics are used as defect signatures.

444 Among the single curve-based methods (M1 and M2), none of them could outperform under all the faulty simulated  
445 conditions. Therefore, an M2-based improved method (NewM2) has been proposed. It has exhibited more robust overall  
446 performance than M1 and M2 with the decrease of average curve error from 3.45% to 2.37%.

447 The method based on multiple curves (M3) generally has higher performance than those based on a single curve, but it is  
448 not suitable for rapid field diagnosis.

449 PV health monitoring and fault diagnosis using I-V curves is a promising approach. However, several signs of progress are  
450 expected from future work to improve its efficiency and ease its implementation. At first, the determination of correction  
451 coefficients based on field-measured data or mitigating the dependence on correction coefficients would be beneficial.  
452 Second, the development of a methodology for automatic determination of reference curves and improved correction  
453 performance (mainly to avoid underestimating incipient faults) under different faulty conditions.

454

## 455 **Acknowledgment**

456 The authors would like to acknowledge the SIRTAs for the field-measured data and the China Scholarship Council (CSC)  
457 for the PhD funding.

## 458 **References**

- 459 Agrawal, N., Bora, B., Kapoor, A., 2020. Experimental investigations of fault tolerance due to shading in photovoltaic  
460 modules with different interconnected solar cell networks. *Sol. Energy* 211, 1239–1254.  
461 <https://doi.org/10.1016/j.solener.2020.10.060>
- 462 Bouaichi, A., Alami, A., Hajjaj, C., Messaoudi, C., Ghennioui, A., Benlarabi, A., Ikken, B., El, A., Zitouni, H., 2019. In-  
463 situ evaluation of the early PV module degradation of various technologies under harsh climatic conditions : The  
464 case of Morocco. *Renew. Energy* 143, 1500–1518. <https://doi.org/10.1016/j.renene.2019.05.091>

465 Bühler, A.J., Perin Gasparin, F., Krenzinger, A., 2014. Post-processing data of measured I–V curves of photovoltaic  
466 devices. *Renew. Energy* 68, 602–610. <https://doi.org/10.1016/j.renene.2014.02.048>

467 Chen, Z., Wu, L., Cheng, S., Lin, P., Wu, Y., Lin, W., 2017. Intelligent fault diagnosis of photovoltaic arrays based on  
468 optimized kernel extreme learning machine and I-V characteristics. *Appl. Energy* 204, 912–931.  
469 <https://doi.org/10.1016/j.apenergy.2017.05.034>

470 Chin, V.J., Salam, Z., Ishaque, K., 2015. Cell modelling and model parameters estimation techniques for photovoltaic  
471 simulator application: A review. *Appl. Energy* 154, 500–519. <https://doi.org/10.1016/j.apenergy.2015.05.035>

472 Ding, K., Zhang, J., Bian, X., Xu, J., 2014. A simplified model for photovoltaic modules based on improved translation  
473 equations. *Sol. Energy* 101, 40–52. <https://doi.org/10.1016/j.solener.2013.12.016>

474 Dolara, A., Lazaroiu, G.C., Leva, S., Manzolini, G., 2013. Experimental investigation of partial shading scenarios on PV  
475 (photovoltaic) modules. *Energy* 55, 466–475. <https://doi.org/10.1016/j.energy.2013.04.009>

476 Fadhel, S., Delpha, C., Diallo, D., Bahri, I., Migan, A., Trabelsi, M., Mimouni, M.F., 2019. PV shading fault detection  
477 and classification based on I-V curve using principal component analysis: Application to isolated PV system. *Sol.*  
478 *Energy* 179, 1–10. <https://doi.org/10.1016/j.solener.2018.12.048>

479 Friesen, G., Herrmann, W., Belluardo, G., Herteleer, B., 2018. Report IEA-PVPS T13-11:2018 Photovoltaic module  
480 energy yield measurements: Existing approaches and best practice, IEA-PVPS. URL [https://iea-pvps.org/wp-](https://iea-pvps.org/wp-content/uploads/2020/01/Photovoltaic_Module_Energy_Yield_Measurements_Existing_Approaches_and_Best_Practice_by_Task_13.pdf)  
481 [content/uploads/2020/01/Photovoltaic\\_Module\\_Energy\\_Yield\\_Measurements\\_Existing\\_Approaches\\_and\\_Best\\_Pr-](https://iea-pvps.org/wp-content/uploads/2020/01/Photovoltaic_Module_Energy_Yield_Measurements_Existing_Approaches_and_Best_Practice_by_Task_13.pdf)  
482 [actice\\_by\\_Task\\_13.pdf](https://iea-pvps.org/wp-content/uploads/2020/01/Photovoltaic_Module_Energy_Yield_Measurements_Existing_Approaches_and_Best_Practice_by_Task_13.pdf) (accessed 6.15.20).

483 Golive, Y.R., Singh, H.K., Kottantharayil, A., Vasi, J., Shiradkar, N., 2019. Investigation of Accuracy of various STC  
484 Correction Procedures for I-V Characteristics of PV Modules Measured at Different Temperature and Irradiances,  
485 in: 2019 IEEE 46th Photovoltaic Specialists Conference (PVSC). IEEE, Chicago, IL, USA, pp. 2743–2748.  
486 <https://doi.org/10.1109/PVSC40753.2019.8980557>

487 Hishikawa, Y., Doi, T., Higa, M., Yamagoe, K., Ohshima, H., Takenouchi, T., Yoshita, M., 2018. Voltage-dependent  
488 temperature coefficient of the I-V curves of crystalline silicon photovoltaic modules. *IEEE J. Photovoltaics* 8, 48–  
489 53. <https://doi.org/10.1109/JPHOTOV.2017.2766529>

490 Hishikawa, Y., Ohshima, H., Higa, M., Yamagoe, K., Doi, T., 2016. Precise Determination of the STC I-V Curves by  
491 Wide-Range Linear Extrapolation of Outdoor I-V Curves on Partly Sunny Days, in: 32nd European Photovoltaic  
492 Solar Energy Conference and Exhibition (Eu-PVSEC). München, Germany, pp. 1716–1719.  
493 <https://doi.org/10.4229/EUPVSEC20162016-5DO.11.4>

494 Hishikawa, Y., Takenouchi, T., Higa, M., Yamagoe, K., Ohshima, H., Yoshita, M., 2019. Translation of Solar Cell  
495 Performance for Irradiance and Temperature from a Single I-V Curve Without Advance Information of Translation  
496 Parameters. *IEEE J. Photovoltaics* 9, 1195–1201. <https://doi.org/10.1109/JPHOTOV.2019.2924388>

497 Huang, J.M., Wai, R.J., Gao, W., 2019. Newly-designed fault diagnostic method for solar photovoltaic generation system  
498 based on IV-Curve measurement. *IEEE Access* 7, 70919–70932. <https://doi.org/10.1109/ACCESS.2019.2919337>

499 Huawei, 2020. Smart I-V Curve Diagnosis. URL [https://solar.huawei.com/en-](https://solar.huawei.com/en-GB/download?p=%2F-%2Fmedia%2FSolar%2Fattachment%2Fpdf%2Feu%2Fdatasheet%2FIV-Curve.pdf)  
500 [GB/download?p=%2F-%2Fmedia%2FSolar%2Fattachment%2Fpdf%2Feu%2Fdatasheet%2FIV-Curve.pdf](https://solar.huawei.com/en-GB/download?p=%2F-%2Fmedia%2FSolar%2Fattachment%2Fpdf%2Feu%2Fdatasheet%2FIV-Curve.pdf)  
501 (accessed 8.17.20).

502 IEC 60891, 2009. Photovoltaic devices - Procedures for temperature and irradiance corrections to measured I-V  
503 characteristics.

504 Li, Y., Ding, K., Zhang, J., Chen, F., Chen, X., Wu, J., 2019. A fault diagnosis method for photovoltaic arrays based on  
505 fault parameters identification. *Renew. Energy* 143, 52–63. <https://doi.org/10.1016/j.renene.2019.04.147>

506 Ma, M., Liu, H., Zhang, Z., Yun, P., Liu, F., 2019. Rapid diagnosis of hot spot failure of crystalline silicon PV module  
507 based on I-V curve. *Microelectron. Reliab.* 100–101. <https://doi.org/10.1016/j.microrel.2019.113402>

508 Martínez-Moreno, F., Figueiredo, G., Lorenzo, E., 2018. In-the-field PID related experiences. *Sol. Energy Mater. Sol.*

509 Cells 174, 485–493. <https://doi.org/10.1016/j.solmat.2017.09.037>

510 Mellit, A., Tina, G.M., Kalogirou, S.A., 2018. Fault detection and diagnosis methods for photovoltaic systems: A review.  
511 *Renew. Sustain. Energy Rev.* 91, 1–17. <https://doi.org/10.1016/j.rser.2018.03.062>

512 Migan, A., Mambrini, T., Bourdin, V., Badosa, J., 2015. Deployment of a multi-technology photovoltaic module test  
513 bench on the SIRTA meteorological and climate observatory, in: 31st European PV Solar Energy Conference and  
514 Exhibition (Eu-PVSEC). Hamburg, Germany.

515 Pillai, D.S., Rajasekar, N., 2018. A comprehensive review on protection challenges and fault diagnosis in PV systems.  
516 *Renew. Sustain. Energy Rev.* 91, 18–40. <https://doi.org/10.1016/j.rser.2018.03.082>

517 Rajput, P., Tiwari, G.N., Sastry, O.S., Bora, B., Sharma, V., 2016. Degradation of mono-crystalline photovoltaic modules  
518 after 22 years of outdoor exposure in the composite climate of India. *Sol. Energy* 135, 786–795.  
519 <https://doi.org/10.1016/j.solener.2016.06.047>

520 Sarikh, S., Raoufi, M., Bennouna, A., Benlarabi, A., Ikken, B., 2020. Implementation of a plug and play I-V curve tracer  
521 dedicated to characterization and diagnosis of PV modules under real operating conditions. *Energy Convers.*  
522 *Manag.* 209. <https://doi.org/10.1016/j.enconman.2020.112613>

523 Silva, A.M., Melo, F.C., Reis, J.H., Freitas, L.C.G., 2019. The study and application of evaluation methods for  
524 photovoltaic modules under real operational conditions, in a region of the Brazilian Southeast. *Renew. Energy* 138,  
525 1189–1204. <https://doi.org/10.1016/j.renene.2019.01.129>

526 Spataru, S., Sera, D., Kerekes, T., Teodorescu, R., 2015. Monitoring and Fault Detection in Photovoltaic Systems Based  
527 On Inverter Measured String I-V Curves, in: 31st European Photovoltaic Solar Energy Conference and Exhibition  
528 (EU PVSEC). Hamburg, Germany, pp. 1667–1674. <https://doi.org/10.4229/EUPVSEC20152015-5BO.12.2>

529 Tanesab, J., Parlevliet, D., Whale, J., Urmee, T., 2017. Seasonal effect of dust on the degradation of PV modules  
530 performance deployed in different climate areas. *Renew. Energy* 111, 105–115.  
531 <https://doi.org/10.1016/j.renene.2017.03.091>

532 Tanesab, J., Parlevliet, D., Whale, J., Urmee, T., Pryor, T., 2015. The contribution of dust to performance degradation of  
533 PV modules in a temperate climate zone. *Sol. Energy* 120, 147–157. <https://doi.org/10.1016/j.solener.2015.06.052>

534 Triki-Lahiani, A., Bennani-Ben Abdelghani, A., Slama-Belkhodja, I., 2018. Fault detection and monitoring systems for  
535 photovoltaic installations: A review. *Renew. Sustain. Energy Rev.* 82, 2680–2692.  
536 <https://doi.org/10.1016/j.rser.2017.09.101>

537 Wang, M., Liu, J., Burleyson, T.J., Schneller, E.J., Davis, K.O., French, R.H., Braid, J.L., 2020. Analytic  
538  $I_{sc}$ – $V_{oc}$  Method and Power Loss Modes From Outdoor Time-Series  $I_{sc}$ – $V_{sc}$  Curves.  
539 *IEEE J. Photovoltaics* 10, 1379–1388. <https://doi.org/10.1109/JPHOTOV.2020.2993100>

540 Zhu, H., Lu, L., Yao, J., Dai, S., Hu, Y., 2018. Fault diagnosis approach for photovoltaic arrays based on unsupervised  
541 sample clustering and probabilistic neural network model. *Sol. Energy* 176, 395–405.  
542 <https://doi.org/10.1016/j.solener.2018.10.054>

543 Zhu, Y., Xiao, W., 2020. A comprehensive review of topologies for photovoltaic I–V curve tracer. *Sol. Energy*.  
544 <https://doi.org/10.1016/j.solener.2019.12.020>

545